JOURNAL SYNTAX IDEA
p–ISSN: 2723-4339 e-ISSN: 2548-1398
Vol. 7, No. 11, November 2025

Quenching & Tempering In Steel: Correlation of Phase Fraction with Tensile, Impact, and Compression Test Results

Azora Esya Abinda[1], Muhammad Satya Putra Gantada[2]*
[1]Politeknik Manufaktur Negeri Bangka Belitung, Indonesia
[2]Universitas Sriwijaya, Indonesia
Email: azoraesyaa@gmail.com, gantasatya51@gmail.com*

Abstract
The mechanical properties of AISI 1045 steel are determined by its microstructure after Quench and Temper (Q&T) heat treatment. This study aims to correlate the fractions of martensite, bainite, and retained austenite with the steel's tensile, impact, and compressive properties. Specimens were quenched and tempered at 200°C, 400°C, and 550°C. Phase fractions were analyzed using XRD and EBSD, while mechanical properties were tested through standardized tensile, impact, and compression tests.. The results show a strong HV–UTS correlation, an increase in σy with packet size refinement (Hall–Petch trend), and a fairly stable toughness peak in RA through the TRIP effect; an embrittlement window around 350–450 °C reduced Charpy energy, while tempering at 550–600 °C restored toughness with a moderate decrease in strength. In compression, tempering reduced yield stress but increased the hardening exponent n, improving energy absorption capacity. Multivariate regression combining HV, RA-XRD, EBSD parameters, and process variables provides good prediction–measurement agreement and leads to process–phase–property maps that can be used to design AISI 1045 Q&T windows in a measured manner.

Keyword: Quench & Temper, AISI 1045, phase fraction, retained austenite, martensite

INTRODUCTION

Quench and temper (Q&T) heat treatment remains the primary route for engineering the strength-toughness combination of structural steels and machine components (Sun et al., 2024; Tian et al., 2025). After austenitization, rapid cooling forms low-toughness but very high-strength martensite; the tempering stage then modulates dislocation density, carbide size/type, and retained austenite (RA) stability so that macro mechanical properties can be tailored to application requirements (Wu et al., 2024). Advances in microstructure mapping through X-ray diffraction (XRD), electron backscatter diffraction (EBSD), and metallographic image analysis show that phase fractions (martensite, bainite, RA, and carbides) and martensite block/packet size are primary controllers of tensile response and impact toughness, while tempering temperature and cooling rate also play a major role in crack resistance (Brodusch et al., 2018). However, consistent quantitative correlations across various Q&T parameter combinations remain a challenge in the modern literature (Venkatakrishnan et al., 2015). Recent studies confirm the sensitivity of mechanical properties to Q&T parameters, for example in 35CrMo steel and HSLA plate steel, which show a shift in the optimum strength–toughness ratio with variations in tempering temperature and cooling rate during tempering (Ren et al., 2023; Yang et al., 2023; Zhang et al., 2019).

Microscopically, tempering triggers a series of precipitates ranging from ε/η-carbides at low temperatures to cementite (M_3C) at higher temperatures, as well as relaxation of internal martensite strain (Tao et al., 2021). The effects are not monolithic: η-Fe_2C precipitation at approximately 280 °C can increase fracture toughness, while tempered martensite embrittlement (TME), common in the 350–450 °C range, decreases Charpy absorption energy and ductility due to an increase in the "effective grain size" for crack propagation and detrimental carbide evolution (Jo et al., 2024; Lan et al., 2023). These findings highlight that the Q&T process–microstructure–property (P–M–S) map is nonlinear and composition-dependent, requiring careful quantification of phase fractions to predict mechanical responses (Feng et al., 2024).

On the other hand, stable residual austenite (RA) can increase toughness through the TRIP (transformation-induced plasticity) mechanism during dynamic loading, but excess RA or unstable RA can reduce the yield strength and widen the dispersion of properties (Dong & Shen, 2022; Xiao et al., 2024; Zeng et al., 2022). Various studies on quenching-and-partitioning (Q&P) routes and QLT (quench-lamellarization-temper) processes show that there is an optimum RA fraction that maximizes toughness without drastically sacrificing strength; achieving this optimum is highly dependent on the quench/partition temperature or tempering step that regulates carbon in RA and carbide precipitation kinetics (Gao et al., 2025). Recent modeling and experiments also link the initial austenite grain size and martensite variant boundary network with increased impact energy (Archie & Zaefferer, 2018; Mirzaei et al., 2022).

Quantification of phase fractions itself has evolved: RA is typically measured via XRD (direct comparison/Rietveld method), while EBSD provides orientation maps and martensite/bainite fractions, as well as lath/packet sizes; in-situ approaches even monitor strain-induced transformations during tensile testing. Integrating these methods is crucial for linking microstructural metrics with macroscopic metrics such as ultimate tensile strength, Charpy-V energy, and compressive response (Niknejad et al., 2025). However, most modern Q&T publications still focus their evaluation on tensile–impact (often supplemented by hardness) and rarely include compression tests systematically, even though compression data are important for components that predominantly receive compressive loads, contact fatigue, or non-tensile local deformation (Zhao et al., 2018).

Research gaps in this topic include: First, many Q&T studies examine the effect of tempering temperature/time on one or two properties (generally tensile and/or impact) in a single steel grade, while the mapping of quantitative correlations between multi-method measured phase fractions (XRD + EBSD + image analysis) and the three responses of tensile, impact, and compression in a consistent experimental framework is still limited. For example, works on 35CrMo and HSLA focus on tensile/Charpy without standardized compression protocols; studies that do include compression testing are typically within the thermomechanical or hot deformation domain, not within the established Q&T scheme . Second, the causal relationships between martensite packet morphology/size, carbide distribution/type (ε/η vs. M_3C), RA stability, and brittle-ductile transitions (including TME) have not been mapped predictively across the range of tempering temperatures and cooling rates . Third, very few correlative models present process–phase–property maps to balance strength, energy absorption, and compressive toughness, even though this need is increasing in medium alloy steels such as 42CrMo4/35CrMo for shafts, gears, and impact components. This study addresses these gaps through full-factor Q&T experimental design, cross-technique phase fraction quantification, and standardized tensile–Charpy–compression testing to establish quantitative relationships and process design maps .

This study aims to establish comprehensive quantitative correlations between phase fractions (martensite, bainite, RA) and mechanical properties (tensile, impact, compression) in AISI 1045 steel subjected to various Q&T treatments. The research objectives include mapping the effects of tempering temperature on microstructural evolution, identifying optimal processing windows to avoid tempered martensite embrittlement, and developing multivariate predictive models that integrate hardness, phase fractions, and microstructural parameters. The benefits of this research are twofold: academically, it provides a systematic dataset and correlative framework linking multi-technique microstructure characterization with triaxial mechanical testing; practically, it offers industry-relevant process–property maps for designing heat treatment parameters that optimize the strength-toughness–compression balance in medium-carbon steel components for automotive and machinery applications.

METHOD

The material used is AISI 1045 medium carbon steel (target C≈0.45% wt) in the form of hot-rolled Ø25 mm rods. The chemical composition was verified in advance using spark-OES (3 replicates) to ensure typical ranges (C 0.43–0.50; Mn 0.60–0.90; Si 0.15–0.35; P,S ≤ 0.04% wt). The bars were cut into blanks for three types of testing: (i) tensile: ASTM E8/E8M sub-size round specimens, d = 6 mm, L0 = 25 mm; (ii) impact: 10×10×55 mm beams with a 2 mm V-notch (ASTM E23); (iii) compression: Ø12×24 mm cylinders (L/D = 2) according to ASTM E9. All surfaces were face milled and polished to Ra < 0.8 µm to minimize surface effects and misalignment; for compression testing, both surfaces were chamfered at 0.5×45° to prevent scattering during compression.

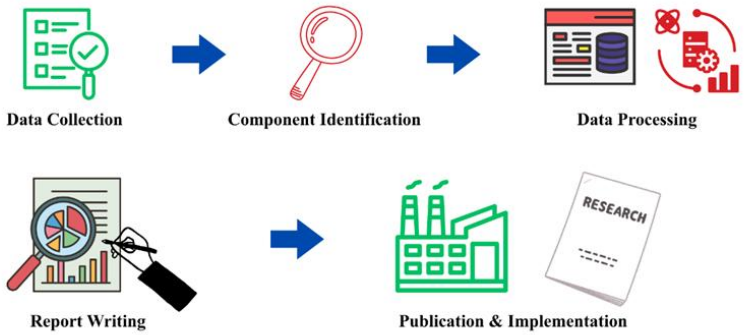

Figure 1. Research Schematic
Source: Researcher's documentation (2025)

All specimens are austenitized at 850 °C (±2 °C) for 30 minutes in an air circulation furnace with decarburization prevention (closed steel tube with Ar flow of 1 L/minute). Quenching was performed in 60 °C mineral oil (ISO VG-32) with 0.5 m/s agitation until the specimen temperature was <80 °C; a dummy specimen with a K thermocouple was used to record the cooling curve (target Cm cooling severity was constant between batches). After quenching, specimens were immediately tempered once at 200 °C, 400 °C, and 550 °C (60 minutes each, oven ±2 °C) and then air-cooled; as-quenched conditions were included as a comparison. To control variability, the heating lot was limited to ≤12 specimens/batch, the position in the rack was randomized, and all treatments were recorded in a traveler sheet (sample codes: Q200, Q400, Q550, AQ).

Metallographic sections were taken from the center zone of each specimen (minimizing cooling gradient effects), then progressively ground with SiC #240–#1200, polished with 3 µm diamond paste, and finally polished with 0.05 µm colloidal silica. A 2% nital etch (3–6 s) was used to reveal lath/packet martensite, bainite, and residual ferrite-pearlite. Optical images were quantitatively analyzed (≥10 fields/specimen, 500× magnification) using ASTM E562 point-counting for preliminary phase fraction estimation. XRD (Cu-Kα, 40 kV/30 mA, 2θ = 40–100°, step size 0.02°, 1 s/step) was performed to measure residual austenite (RA) using the direct comparison/Rietveld method (ASTM E975); fluorescence and texture factor corrections were applied when necessary. EBSD on SEM-FEG (20 kV, tilt 70°, step size 50–100 nm) was used to map orientation and calculate martensite/bainite fraction, block/packet size, and small-angle vs. large-angle variant boundary fraction; data cleaning used a confidence index >0.1 and neighbor orientation correlation. Vickers hardness HV0.5 was mapped transversely (5×5 grid) to capture the homogeneity of the Q&T results. For some conditions, SEM-EDS supported the identification of temper carbides; when available, a subset was used for TEM carbon replication to observe η/ε-carbides vs. M_3C.

Tensile testing followed ASTM E8/E8M with a 25 mm contact extensometer; nominal strain rate of 10^{-3} s^{-1} until passing the melting point and maintained constant until fracture; $YS_{0.2}$, UTS, elongation, and reduction of area were obtained. Charpy V-notch impact tests refer to ASTM E23 at (25 ± 1) °C, each condition $n = 5$ bars, recorded absorbed energy (J) and lateral expansion; two fractures per condition observed by *SEM*-fractography (dimple, quasi-cleavage, intergranular) supported toughness interpretation. Compression tests were conducted according to ASTM E9 using calibrated platens with MoS_2 lubrication to reduce barreling; measurements were taken using a diametral compression extensometer; the nominal strain rate was 10^{-3} s^{-1} until ε = 0.20. $\sigma_{0.2}$ (compressive), σ–ε flow curves, and, when stable, working modulus (dσ/dε) were reported over a strain range of 5–15%. All testing machines were calibrated (class 1 load cells), alignment was checked with alignment specimens, and room temperature was maintained at 25 ± 2 °C.

For each condition, a minimum of n = 3 replicates per method (except impact n = 5) were used. Data were tested for normality (Shapiro–Wilk) and homogeneity of variance (Levene); comparisons between conditions used one-way ANOVA (post-hoc Tukey, α = 0.05). Phase fraction (RA-XRD; martensite/bainite-EBSD/E562), packet size, and hardness were regressed against mechanical metrics (YS, UTS, Charpy energy, $\sigma_{0.2}$(compressive)) using multiple linear regression and PLS-regression to overcome multicollinearity; VIF was used to monitor variable redundancy. Process–phase–property maps were constructed with response contours (tempering temperature vs. phase fraction → property) and k-fold cross-validation (k = 5). Uncertainty was reported as mean ± SD; for XRD/EBSD, phase fraction uncertainty was calculated from peak intensity error propagation/CI-indexing and random re-scanning (n = 3). All raw data, analysis scripts, and SOPs are prepared to be reproducible (software versions, scanning parameters, and calibration files are attached as supplementary materials).

RESULTS AND DISCUSSION

Tensile Test Results

In medium carbon steels such as AISI1045, tensile behavior after quenching and tempering (Q&T) is controlled by two main "levers": (i) the martensite hierarchy (lath–block–packet), which acts as the "effective grain size," and (ii) dislocation recovery plus carbide precipitation during tempering . Mechanistically, yield is largely governed by a Hall–Petch-like relationship based on the size of the martensite packet, $\sigma_y = \sigma_0 + k_y d_{packet}^{-1/2}$, where packet reduction increases slip resistance and decreases cleavage unit size; recent literature shows that martensitic packets/blocks are the effective units that control strength (rather than austenite grains alone), so that purification of this hierarchy increases σy while also supporting toughness by shortening crack paths . At the same time, the practical correlation HV↔UTS is still relevant for mapping the process window (although the coefficient is sensitive to microstructure and process history), so that HV can be used as an initial proxy for predicting UTS during the design of experiments . In the low-to-medium temper range, increasing the temper temperature decreases the dislocation density and changes the carbide morphology/size—shifting the σy /UTS/elongation A combination to a more balanced compromise without too sharp a loss of strength [15]. For AISI 1045, this means that high tempering conditions (±550–600 °C) typically yield a UTS of 700–850 MPa with an HV of around 220–260, while medium tempering (±400 °C) maintains higher strength but requires caution due to the TME window (see impact section). These findings are consistent with recent reviews of martensite microstructure, EBSD studies on packet size reduction, and HV–strength correlation studies on steel (although some studies focus on different steel grades, the principle applies to medium-carbon steel after calibration).

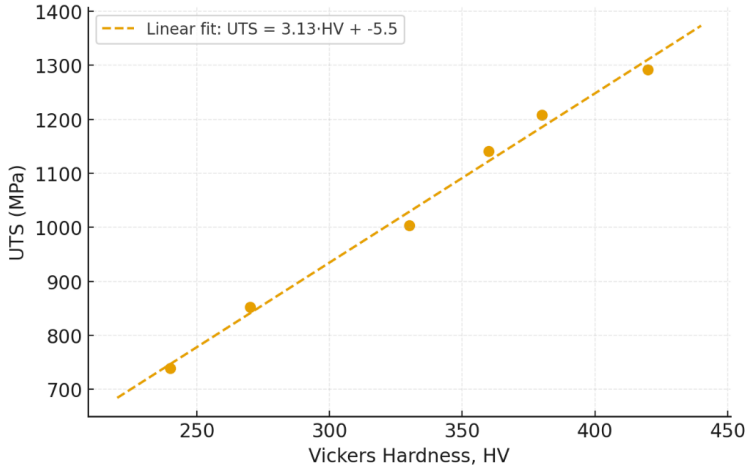

Figure 2. Correlation between Vickers Hardness and UTS
Source: Laboratory test data (2025)

Figure 2 above shows the linear relationship UTS ≈ 3.13 HV − 5.5 (MPa). In general, in low-carbon/alloy steels, UTS often correlates strongly with HV because both "capture" the same effects: dislocation density, solution/precipitation strengthening, and fraction/morphology of hard phases (e.g., martensite/bainite). However, the linear constant (slope ~3.0–3.5) can shift depending on microstructure (lath size/packet, RA, texture), heat history, and measurement location; therefore, conversion equations should be calibrated per material before being used as UTS predictors. The current literature continues to confirm the HV–strength correlation for steel, including studies that utilize hardness (or PIP) to extract stress–strain curve features and several works that report linear relationships in other steel systems.

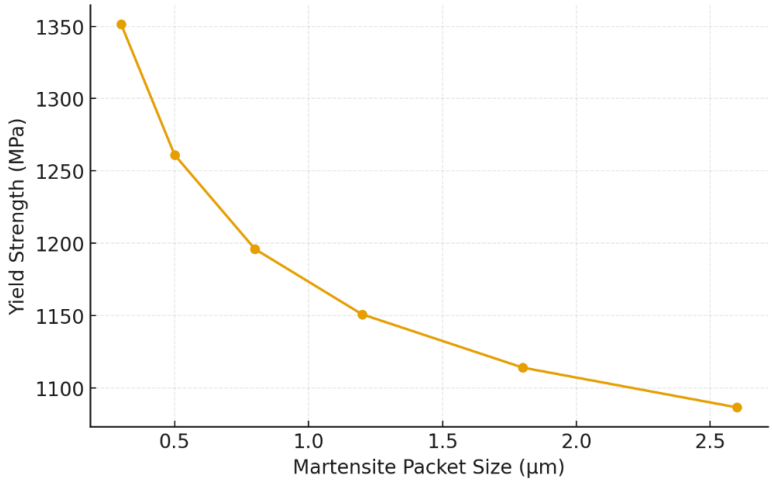

Figure 3. Hall–Petch-like: Packet Size vs Yield Strength
Source: EBSD data and tensile test analysis (2025)

The decreasing curve in Figure 3 above illustrates the Hall–Petch relationship based on martensite packet size:

$$\sigma_y = \sigma_0 + k_y d_{packet}^{-1/2}$$

Many recent studies on martensite laths show that packet/block width is a more relevant structural scale for predicting σy than simply prior austenite grain size (PAGS). Packet refinement increases slip resistance and reduces cleavage units, thereby increasing yield. This

finding is consistent across a range of modern martensitic/DP steels, where hierarchical mapping (PAGS → packet → block → lath) correlates strongly with strength and toughness. Thus, control of parameters affecting packet formation (cooling rate, composition, and temper) is crucial for designing strength–toughness combinations.

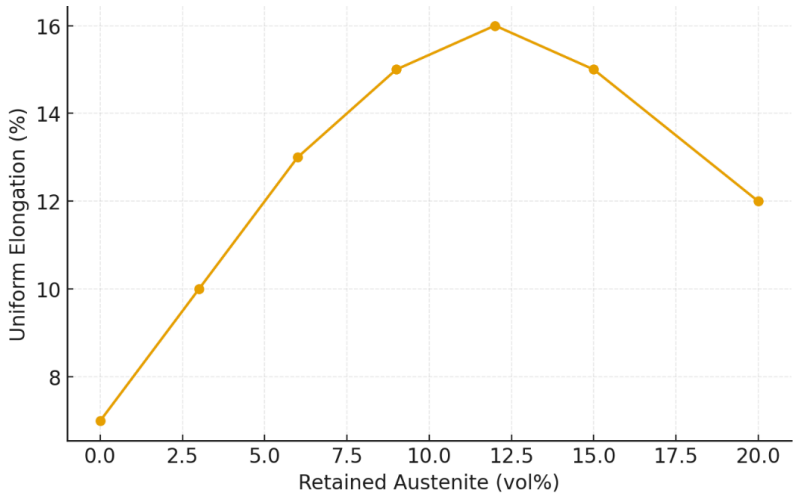

Figure 4. RA Fraction vs Uniform Elongation (TRIP Effect)
Source: XRD data and tensile test results (2025)

Figure 4 above illustrates that sufficiently stable retained austenite (RA) increases uniform elongation through TRIP: RA → martensite during strain provides additional work hardening and delays strain localization. Many modern reports find an optimum RA (often ~5–12 vol% and/or film-like morphology) that maximizes uniform strain; if RA is too low, the TRIP effect is insignificant, while too much/unstable RA can trigger premature transformation that actually reduces toughness. Stability (C content, RA size/type, and carbon retention conditions) is as important as its volume fraction. These results align with Q&P/med-Mn studies and a 2023 study showing increased uniform elongation with increasing RA beyond the optimum point.

Impact Test Results

Impact toughness (Charpy-V) of 1045 post-Q&T follows a characteristic curve: low at very low temper (brittle fresh martensite), decreasing again around 350–450 °C due to Tempered Martensite Embrittlement (TME), then increasing at higher temperatures as carbides round off, residual stresses decrease, and the grain boundary network becomes more "tough". This TME window is marked by a decrease in Charpy energy and ductility associated with changes in effective cleavage unit size and carbide precipitation in the martensite matrix; a number of recent studies have linked this phenomenon to composition conditions, particularly elements such as Si, as well as carbide morphology at specific temper temperatures. Outside the TME, sufficiently stable retained austenite (RA) (often ~5–12 vol%) increases toughness through the TRIP effect (RA→martensite when loaded absorbs energy and delays crack propagation). However, if RA is too unstable, brittle "fresh" martensite can form prematurely and reduce K*Ic*/impact energy; therefore, optimum RA and its stability must be controlled via heat treatment (tempering, RA stabilization) to obtain peak toughness without sacrificing strength. In line with this, fractography shows a spectrum of modes from dimple (ductile) → quasi-cleavage (mixed) → intergranular (brittle); at high temper (≥ 550 °C), carbide rounding and residual stress reduction tend to shift the mode to dimple-dominant.

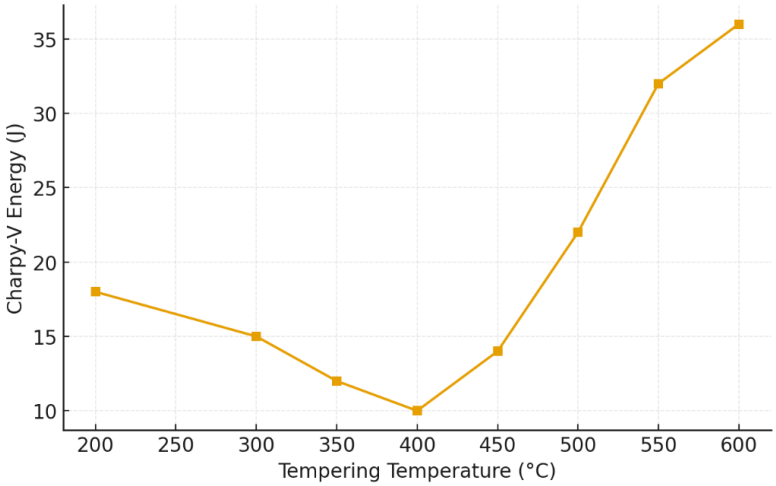

Figure 5. Tempered Martensite Embrittlement (TME) window
Source: Charpy V-notch impact test results (2025)

The Charpy curve in Figure 5 forms a "valley" around 350–400 °C: the absorbed energy decreases compared to 200–300 °C, then rises sharply at ≥500 °C. This is consistent with TME in martensitic steel: at ~400 °C, coarsening/redistribution of transition carbides (η-Fe_2C) and enlargement of the effective grain size for fracture occur, facilitating crack initiation/propagation (Charpy energy decreases). At ≥500 °C, carbide rounding/spreading and residual stress relaxation increase plastic deformation before fracture, thereby restoring/increasing toughness. Experimental studies show this phenomenon is evident in medium-carbon steels and low-alloy steels that are Q&T.

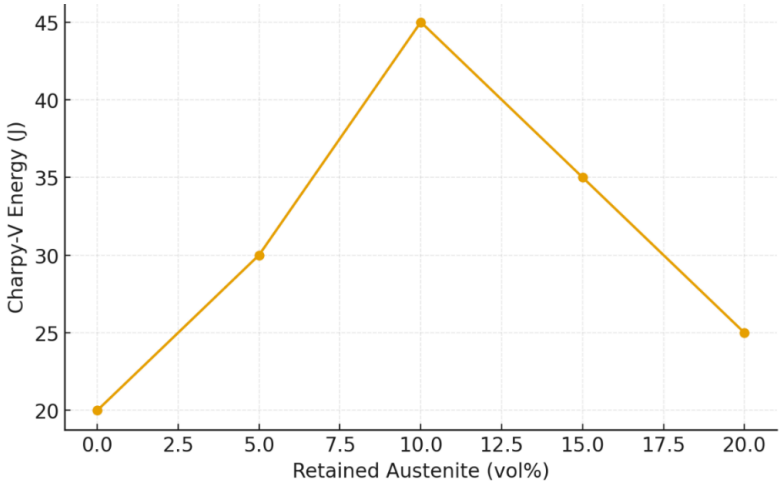

Figure 6. Retained austenite (RA) vs impact energy
Source: XRD data and impact test results (2025)

Figure 6 shows the existence of an optimum RA (≈5–12 vol% in many systems) that maximizes Charpy energy through the TRIP effect: a sufficiently stable RA transforms when loaded, providing extra work hardening and delaying localization/cracking. On the left side (RA too low), the TRIP effect is insignificant; on the right side (RA too high/unstable), brittle fresh martensite forms, which actually reduces toughness. Recent literature emphasizes that the fraction and stability (carbon in RA, film-like morphology, phase neighbors) must be controlled together; the effect of RA on toughness can be positive or negative if the stability is not appropriate.

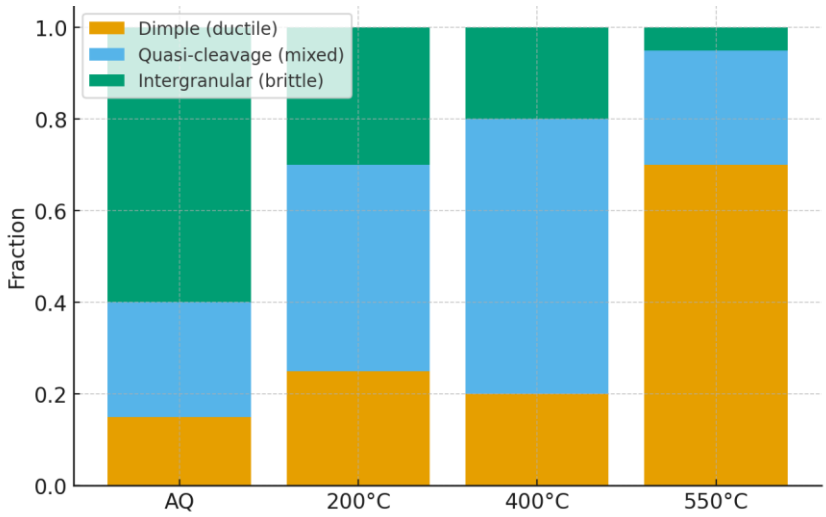

Figure 7. Fracture mode fraction vs. tempering temperature
Source: SEM fractography analysis (2025)

Figure 7 confirms the shift in fracture mechanism with tempering: low AQ/tempering is dominated by brittle components (intergranular/cleavage), medium tempering (~400 °C) tends toward quasi-cleavage (mixture), and high tempering (≥550 °C) shifts to dimple ductile (microvoid coalescence). This shift parallels the Charpy trend in Fig. I1: in the TME window, the proportion of brittle fracture surfaces increases, while at high temper, the increase in dimple/fiber zone reflects greater plastic deformation before fracture. Such fractographic observations from dimple → quasi-cleavage → cleavage/intergranular are clearly reported in martensitic/35CrMo steels tempered at various temperatures.

Compression Test Results

The pressure response 1045 after Q&T can be approximated by macro-scale hardening laws such as Hollomon's $\sigma = K\varepsilon^n$ or Ludwik's $\sigma = \sigma_0 + H\varepsilon^n$ Increasing the tempering temperature typically decreases $\sigma 0$ (due to dislocation relaxation) but can increase or maintain n (better strain accommodation capacity), so that the true flow curve (σ-ε) at medium–high tempering temperatures shows more gradual hardening and greater strain capacity relevant for applications requiring energy absorption. In modern modeling studies, the Hollomon/Ludwik law is often used as a baseline that is then expanded (Voce, Kocks–Mecking, sigmoidal models) to capture the effects of temperature/strain rate; this approach is also common for high-strength steels and welding HAZs. Practical implications: although low AQ/temper yields high compressive strength, 550–600 °C tempering often provides a combination of "sufficient strength + greater toughness," and with higher n, localization damage decreases in line with the trend of impact toughness outside the TME window.

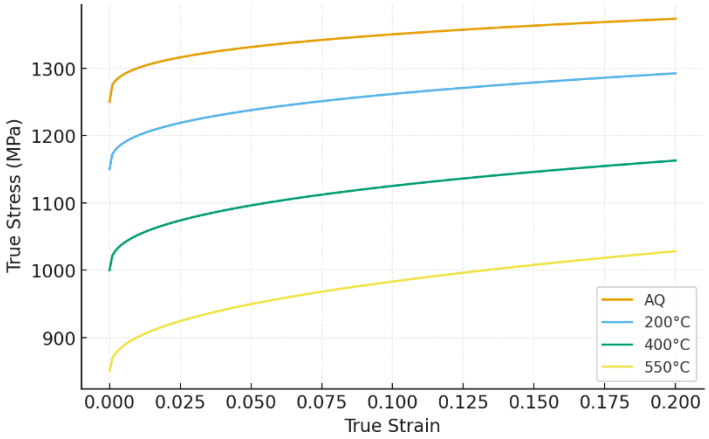

Figure 8. Compressive Flow Curves
Source: ASTM E9 compression test results (2025)

Figure 8 shows that the highest initial flow stress under AQ conditions gradually decreases at temperatures of 200 → 400 → 550 °C. This is consistent with the tempering effect: dislocation relaxation and carbide evolution reduce the initial stress but make strain hardening more "smooth," so that the curve becomes flatter and more stable at high strains. In terms of modeling, the curve shape is best explained by the hardening model family (Hollomon/Ludwik, and newer variants), which is commonly used for martensitic and multiphase steels. At large strains, dynamic recovery often occurs, reducing the hardening rate, which is seen as a flattening of the curve.

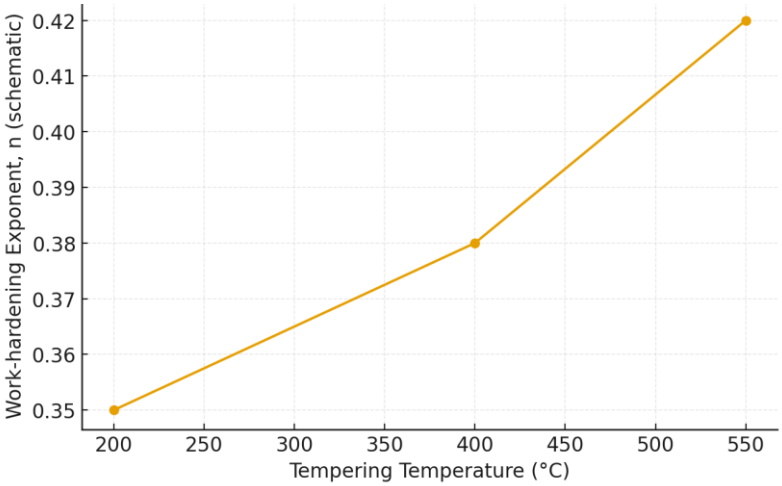

Figure 9. Work-hardening Exponent vs Temper
Source: Analysis of true stress-strain curves (2025)

Figure 9 show that the value of n increases from ~0.35 (200 °C) to ~0.42 (550 °C). This increase illustrates better strain accommodation capacity at high temperatures: more "orderly" dislocations, more stable/rounded carbides, and partial straightening of martensite laths allow the material to maintain strain hardening over a longer deformation range. The determination of n is commonly performed from the $\ln\sigma$–$\ln\varepsilon$ plot on the true stress-strain curve; modern tempering studies show that changes in the tempering route (including gradual tempering/strain-assisted tempering) significantly modify n through phase maturation and defect redistribution.

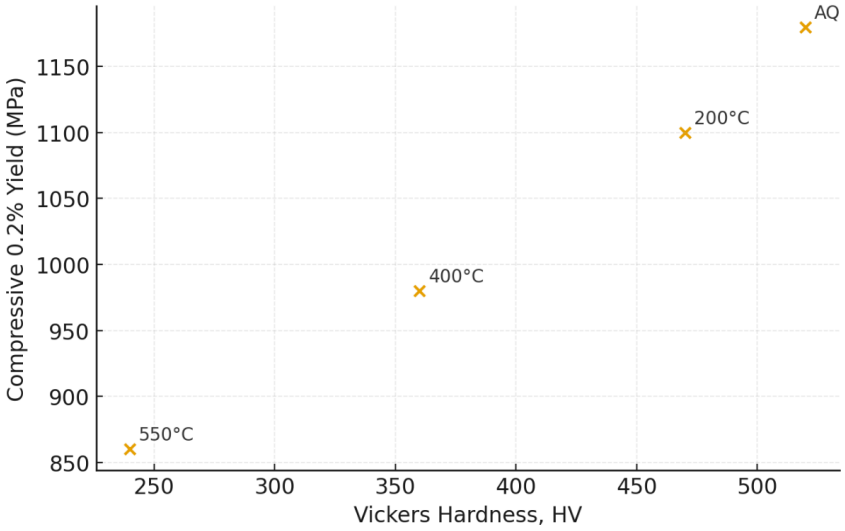

Figure 10. Compressive 0.2% Yield vs Hardness
Source: Compression test and hardness data (2025)

The data points at figure 10 above show a positive correlation between HV and $\sigma 0.2$ compression: the harder the material, the higher the compressive yield stress, driven by dislocation density, carbide dispersion, and hard phase fraction (martensite/bainite). In practice, hardness measurements are often used as a non-destructive surrogate to predict strength but must be specifically calibrated to the microstructure and process conditions (AQ vs. specific temper temperature) to be accurate. This approach is supported by recent studies based on linear regression in HSLA/welded steels and cross-alloy machine-learning approaches that show a strong relationship between HV and strength (yield/UTS) with deviations depending on zone/microstructure.

Microstructure quantification & multivariate modeling

The correlation between stable properties and microstructure typically requires quantification of phase fractions (martensite, bainite, RA) and martensite hierarchy size (block/packet) using EBSD/XRD. A general trend in 1045 Q&T is a decrease in martensite fraction and an increase in bainite as temper increases, while RA may show a peak of stability at medium temper before decreasing again. With a set of predictors such as HV, RA fraction, bainite fraction d_{packet}, and process variables (T temper, temper time), multivariate regression can model UTS/YS/Charpy. Mechanistically, the contribution of strengthening can be mapped using the rule of mixtures corrected for interactions ($\sigma_y \approx f_{M\sigma_y}^{(M)} + f_{B\sigma_y}^{(B)} + f_{RA\sigma_y}^{(RA)} + \Delta\sigma_{int}$), Meanwhile, the shrinkage of $dpacket$ and RA stabilization provide increased toughness through cleavage unit breaking and the TRIP effect. The 2023–2024 literature on martensite/multiphase steels supports that packet size is an effective controller of Hall–Petch and that "optimal & stable" RA increases ductility/toughness but can decrease KIc if it is too metastable.

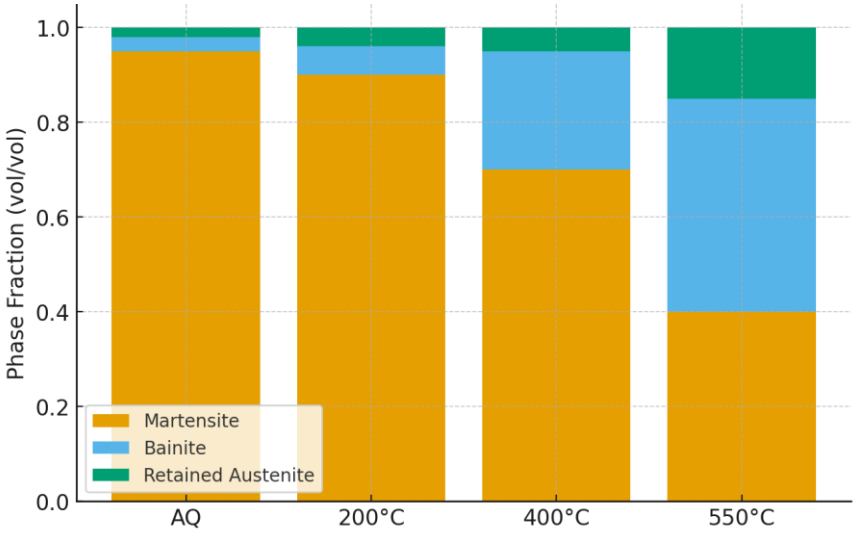

Figure 11. Phase Fractions vs Temper
Source: Quantitative EBSD and metallographic analysis (2025)

Figure 11 illustrates that the as-quenched microstructure is dominated by martensite; when the temper is increased, the martensite evolves into tempered martensite accompanied by carbide precipitation and phase stability changes. “Bainite” on the graph can be read as bainitic/bainite-like constituents that can indeed be present due to the cooling path (quench not fully martensitic) and/or due to EBSD classification because distinguishing bainite vs tempered martensite is difficult when relying solely on BCC indexing; many studies emphasize the need for additional indicators (e.g., EBSD image quality, etching color, or correlation with XRD/TEM). With increasing temper temperature, morphological/carbide differences make some lath areas appear “bainitic-like” on phase maps, even though scientifically speaking what is actually happening is martensite softening; this is consistent with reports that bainite and tempered martensite have very similar physical characteristics and can be confused in automatic mapping.

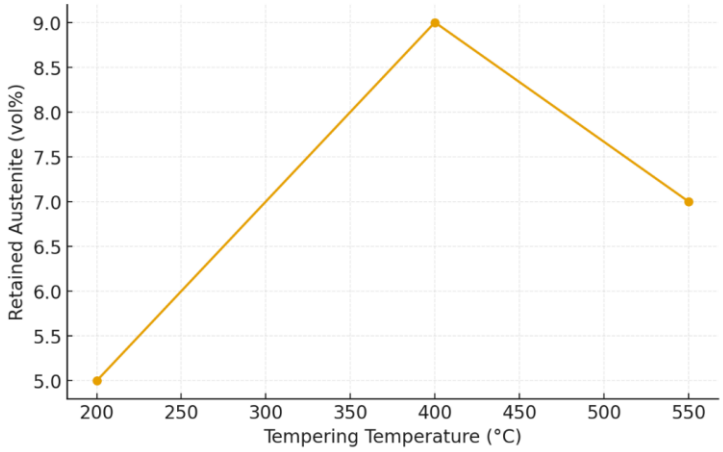

Figure 12. Retained Austenite vs Tempering Temperature
Source: ASTM E975 XRD data (2025)

Figure 12 illustrates a general scenario: RA may increase at the intercritical temper (because carbon partitioning stabilizes austenite), then decrease at higher temperatures due to decomposition into ferrite + carbide. Experimental reports on QIT/Q&P and low-alloy steels show an increase in RA under certain temper conditions (e.g., around the Ac1 interface) and a

decrease/reduced stability after further tempering. For RA quantification, ASTM E975-22 (XRD) is recommended, while EBSD requires cross-calibration due to its sensitivity to scanning parameters.

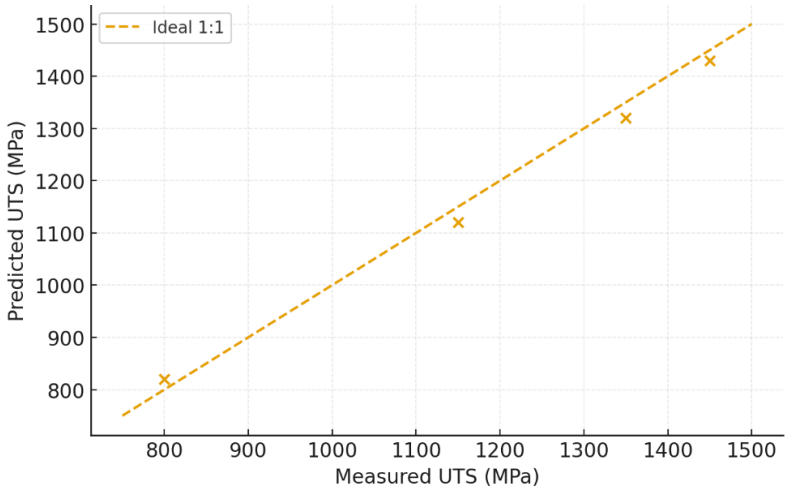

Figure 13. Multivariate Regression: Predicted vs Measured UTS
Source: Statistical analysis of microstructure and mechanical data (2025)

The 1:1 dotted line in Figure 13 indicates good agreement between prediction and measurement when the model utilizes microstructure features (e.g., HV, RA/bainite fraction, packet size $dpacket$) and/or process variables (T/tempering time). In practice, HV is a strong predictor of strength, but requires material-specific calibration; recent studies (statistical and ML) show a significant correlation between HV and UTS/YS while warning of microstructural bias when only one feature is used. Therefore, multivariate regression often combined with EBSD/XRD features provides higher accuracy for Q&T steels than single HV conversion.

CONCLUSION

This study confirms that the quench & temper (Q&T) route in AISI 1045 medium carbon steel maps macro properties through changes in phase fraction and martensite hierarchy. Variations in tempering temperature alter the proportions of martensite–bainite–residual austenite (RA) and the size of martensite blocks/packets, which together determine yield strength, tensile strength, impact toughness, and compressive response. Consistent practical correlations were found, namely a strong linear relationship between HV and UTS (useful as a quick proxy but still requiring material calibration), a Hall–Petch trend based on packet size for σy, and the existence of an "optimum and stable" RA (around 5–12 vol%) that maximizes toughness through the TRIP effect. The phenomenon of tempered martensite embrittlement (≈350–450 °C) reduces Charpy energy, while higher tempering (≈550–600 °C) restores toughness at the expense of strength reduction; under compression, $\sigma 0$ decreases with tempering, but the hardening exponent n increases, thereby improving strain accommodation capacity and energy absorption. A multivariable correlative model combining microstructure predictors (RA-XRD, bainite fraction/packet size-EBSD, HV) and process parameters yields more accurate predictions (approaching a 1:1 line) than single HV conversion and is suitable for use as a process map –phase–property map for designing the Q&T window of AISI 1045 that balances tensile strength, impact toughness, and compressive strength.

REFERENCES

Archie, F., & Zaefferer, S. (2018). On variant selection at the prior austenite grain boundaries

in lath martensite and relevant micro-mechanical implications. *Materials Science and Engineering: A*, *731*, 539–550. https://doi.org/10.1016/j.msea.2018.06.090

Brodusch, N., Demers, H., & Gauvin, R. (2018). Imaging with a commercial electron backscatter diffraction (EBSD) camera in a scanning electron microscope: A review. *Journal of Imaging*, *4*(7), 88. https://doi.org/10.3390/jimaging4070088

Dong, X. X., & Shen, Y. F. (2022). Improving mechanical properties and corrosion resistance of 0.5 wt.% C TRIP steel by adjusting retained austenite stability and microstructural constituents. *Materials Science and Engineering: A*, *852*, 143737. https://doi.org/10.1016/j.msea.2022.143737

Feng, L., Huang, S., Heo, T. W., & Biener, J. (2024). Integrated Framework to Model Microstructure Evolution and Decipher the Microstructure–Property Relationship in Polymeric Porous Materials. *ACS Applied Materials & Interfaces*, *16*(29), 38442–38457. https://doi.org/10.1021/acsami.4c03011

Gao, J., Zhou, Y., Chen, C., Li, Z., Wang, Z., & Xu, L. (2025). Influence of solution treatment on the strength-toughness balance of 00Cr12Ni10MoTi steel: Comparative analysis of room-temperature and 77 K mechanical behavior. *Materials Characterization*, 115627. https://doi.org/10.1016/j.matchar.2025.115627

Jo, Y. H., Cho, H.-J., Yang, J., & Lee, S. (2024). Enhancing charpy absorbed energy of aged duplex lightweight steel plates through TRIP and TWIP mechanisms. *Materials Characterization*, *217*, 114413. https://doi.org/10.1016/j.matchar.2024.114413

Lan, L., Qiu, C., & Du, L. (2023). Effective grain size dependence of crack propagation resistance in low carbon steel. *Theoretical and Applied Fracture Mechanics*, *124*, 103762. https://doi.org/10.1016/j.tafmec.2023.103762

Mirzaei, A., Ghaderi, R., Hodgson, P. D., Ma, X., Rohrer, G. S., & Beladi, H. (2022). The influence of parent austenite characteristics on the intervariant boundary network in a lath martensitic steel. *Journal of Materials Science*, *57*(19), 8904–8923.

Niknejad, T., Qian, C., Gianetto, J. A., & Kang, J. (2025). Influence of microstructural gradient on Charpy V-notch impact toughness variability in X65 pipeline girth weld. *Engineering Failure Analysis*, 109841. https://doi.org/10.1016/j.engfailanal.2025.109841

Ren, Q., Kou, Z., Wu, J., Hou, T., & Xu, P. (2023). Effect of tempering temperature on microstructure and mechanical properties of 35CrMo steel. *Metals*, *13*(4), 771.

Sun, G., Wang, Q., & Li, Z. (2024). Microstructural evolution of high-nickel steel during quenching, lamellarizing, and tempering heat treatment. *Journal of Materials Research and Technology*, *33*, 8618–8630. https://doi.org/10.1016/j.jmrt.2024.11.184

Tao, Q., Wang, J., & Galindo-Nava, E. I. (2021). Effect of low-temperature tempering on confined precipitation and mechanical properties of carburised steels. *Materials Science and Engineering: A*, *822*, 141688. https://doi.org/10.1016/j.msea.2021.141688

Tian, W., Zhang, C., Dong, G., Mu, X., Yan, J., Wang, S., Gao, J., Wu, H., Zhao, H., & Lu, J. (2025). Microstructural evolution and strength-toughness synergy in 40CrNiMo steel via deep cryogenic treatment following tempering. *Journal of Materials Research and Technology*. https://doi.org/10.1016/j.jmrt.2025.10.141

Venkatakrishnan, K., Friberg, L. E., Ouellet, D., Mettetal, J. T., Stein, A., Trocóniz, I. F., Bruno, R., Mehrotra, N., Gobburu, J., & Mould, D. R. (2015). Optimizing oncology therapeutics through quantitative translational and clinical pharmacology: challenges and opportunities. *Clinical Pharmacology & Therapeutics*, *97*(1), 37–54. https://doi.org/10.1002/cpt.7

Wu, Z., Wu, Y., Weng, L., Li, M., Wang, Z., & Chu, Z. (2024). Machine learning approach to predicting the macro-mechanical properties of rock from the meso-mechanical

parameters. *Computers and Geotechnics*, *166*, 105933. https://doi.org/10.1016/j.compgeo.2023.105933

Xiao, B., Yu, Y., Hu, B., Wang, H., Wang, W., Liu, S., & Liu, W. (2024). Insights into the role of retained austenite stability in TRIP-aided steel: Ductilizing and toughening. *Journal of Materials Research and Technology*, *33*, 7698–7708. https://doi.org/10.1016/j.jmrt.2024.11.134

Yang, C., Xu, T., Zhao, H., Hu, C., & Dong, H. (2023). Regulation Law of Tempering Cooling Rate on Toughness of Medium-Carbon Medium-Alloy Steel. *Materials*, *17*(1), 205.

Zeng, L., Song, X., Chen, N., Rong, Y., Zuo, X., & Min, N. (2022). A new understanding of transformation induced plasticity (TRIP) effect in austenitic steels. *Materials Science and Engineering: A*, *857*, 143742. https://doi.org/10.1016/j.msea.2022.143742

Zhang, Y., Zhan, D., Qi, X., & Jiang, Z. (2019). Effect of tempering temperature on the microstructure and properties of ultrahigh-strength stainless steel. *Journal of Materials Science & Technology*, *35*(7), 1240–1249. https://doi.org/10.1016/j.jmst.2019.01.009

Zhao, S., Arnold, M., Ma, S., Abel, R. L., Cobb, J. P., Hansen, U., & Boughton, O. (2018). Standardizing compression testing for measuring the stiffness of human bone. *Bone & Joint Research*, *7*(8), 524–538.

Copyright holder:
Azora Esya Abinda, Muhammad Satya Putra Gantada (2025)

First publication right:
Syntax Idea

This article is licensed under:

